Volumetric digital image correlation applied to X-Ray microtomography images form triaxial compression tests on argillaceaous rocks

Nicolas Lenoir, Michel Bornert, Jacques Desrues, Pierre Bésuelle, Gioacchino Cinno Viggiani

Volumetric Digital Image Correlation Applied to X-ray Microtomography Images from Triaxial Compression Tests on Argillaceous Rock

N. Lenoir*†, M. Bornert‡, J. Desrues†, P. Bésuelle† and G. Viggiani†

*ANDRA, Châtenay-Malabry, France

†Laboratoire 3S, CNRS-UJF-INPG, B.P. 53, 38041 Grenoble,

‡France LMS, Ecole Polytechnique, Palaiseau, France

ABSTRACT: A set of triaxial compression tests on specimens of argillaceous rock were performed under tomographic monitoring at the *European Synchrotron Radiation Facility* in Grenoble, France, using an original experimental set-up developed at *Laboratoire 3S*, Grenoble. Complete 3D images of the specimens were recorded throughout each test using X-ray microtomography. Such images were subsequently analysed using a Volumetric Digital Image Correlation software developed at the *Laboratoire de Mécanique des Solides* in Palaiseau, France. Full-field incremental strain measurements were obtained, which allow to detect the onset of shear strain localisation and to characterise its development in a 3D complex pattern. Volumetric Digital Image Correlation revealed patterns which could not be directly observed from the original tomographic images, because the deformation process in the zones of localised deformation was essentially isochoric (i.e. without volu-metric strain), hence not associated to density changes.

KEY WORDS: *clayey rocks, digital image correlation, failure, localization, triaxial compression test, X-ray tomography*

NOTATION

I	intensity of attenuated X-rays
I_0	initial intensity of X-rays
x	path length of X-rays
μ	linear attenuation coefficient
ρ	local density
Z	atomic number
E	energy of the X-rays
a, b	instrument-dependent parameters
$f(x)$	grey level in reference image at point x
$g(x)$	grey level in deformed image
Φ	local transformation
$C(\Phi)$	correlation coefficient
D	correlation window
N	number of voxels in D
n_x, n_y, n_z	width, height and depth of correlation window
s_x, s_y, s_z	width, height and depth of exploration window
$\langle a \rangle$	average of quantity a over D
a_{ijk}	value of quantity a at voxel (i, j, k)
$E(a)$	integer part of a
ε	strain tensor
dev(ε)	deviatoric part of strain tensor
ε_{eq}	von Mises equivalent strain
σ_u	standard deviation on displacements errors
L	local gauge length
m	number of independent relative displacement evaluations used in strain calculation

Introduction

In the framework of underground nuclear waste disposal studies, an experimental programme was performed at Laboratoire 3S (Grenoble, France), specifically investigating strain localisation in argillaceous rocks. The objective of the project, partly funded by ANDRA (*Agence Nationale pour la Gestion des Déchets Radioactifs*, French Agency for nuclear waste disposal), was to evaluate the excavation-induced deformation in the rock around a gallery. Upon excavation, an 'Excavation Damaged Zone' is created, in which the originally low permeability of the host rock may be modified by the development of strain localisation. Strain localisation is a phenomenon affecting a wide class of both natural and man-made materials, by which an initially homogeneous, or *diffuse*, deformation process turns into a highly concentrated

deformation process, in the form of shear bands [1, 2]. Eventually, shear bands can give rise to the development of cracks and finally fractures in the material. Strain localisation is a *multi-scale* phenomenon, which can be observed in nature from a kilometre scale (faults) down to the metre scale (on outcrops and cliffs), and in the laboratory from the millimetre down to the micrometre scale. In order to improve the understanding and modelling of strain localisation, the onset and development of this phenomenon must be studied experimentally.

A number of studies have been devoted to strain localisation in geomaterials in the past. Full-field measurement methods have been used, mostly on 2D images from plane strain tests, e.g. by Desrues *et al.* (see Ref. [3] for a review) using false relief stereophotogrammetry, but also in 3D tests using X-ray tomography [4, 5]. These studies were mainly conducted on granular, coarse-grained materials (e.g. sand). As far as X-ray tomography is concerned, for a long time its spatial resolution was not sufficient to study localised deformation processes in fine-grained geomaterials (e.g. clays and clayey rocks). However, this has now become possible thanks to the development of X-ray *micro*tomography [6].

In the present study, an argillaceous rock (Callovo-Oxfordian argillite) was tested in the laboratory at stress levels which are representative of the deep underground conditions, where principal effective stresses are on the order of 10 MPa. This required the use of equipment allowing for confined tests with independent control of isotropic and deviatoric components of the applied stress. The onset and development of strain localisation in the argillite specimens were studied using X-ray microtomography at the *European Synchrotron Radiation Facility* (ESRF) in Grenoble, France. It is important to stress that tomography was performed *in situ*, i.e. the specimens were scanned at the ESRF *during loading*. This required the design of a loading system which could be placed in the X-ray beam.

The tomographic images were then analysed in detail by means of Volumetric Digital Image Correlation techniques (3D-DIC, hereafter) based on the natural contrast of such rocks, which is provided by their composite microstructure. In the paper, 3D imaging and image processing are first addressed. Then, the results are presented from a test performed under 10 MPa confining pressure. An important issue with using 3D-DIC to detect strain localisation is that, depending on the stress conditions, the deformation process in a rock may be isochoric, which means that the isotropic (volumetric) part of the deformation is negligible. In this case, direct observation of the tomographic images does not allow detecting strain localisation, as deviatoric deformation does not induce any change in the local mass density. Hence, 3D-DIC of tomographic images is a very significant advance as a measuring technique for localised deformation in geomechanics. The accurate detection of pure shear localised modes, without any dilatancy or crack opening is a crucial issue for underground waste disposal security. In fact, such localised deformation structures are found to open up upon a release of the isotropic stress, with a significant increase of the overall rock permeability.

Materials and Methods

X-ray tomography

X-ray computed tomography (XR-CT) is a technique that allows non-destructive imaging and quantification of internal features of an object in 3D. The method reveals differences in density and atomic composition. First developed for medical imaging, XR-CT is now widely used in material sciences and proved its interest in various domains of geosciences [7, 8]. The principle of the measurement consists in recording X-ray radiographic images of a specimen at several different angular positions. From these different projections, virtual slices can be reconstructed with appropriate algorithms that are either algebraic or based on a back projection principle. Stacking several sequential slices then allows for reconstructing a three-dimensional image of the object. The reconstruction of the slices is based on the spatial distribution of the linear attenuation coefficient, which is determined by using the well-known Beer–Lambert's law:

$$I = I_0 \ \exp(-\mu x) \tag{1}$$

where I_0 and I are, respectively, the initial intensity of X-rays and the X-ray intensity measured after passing the object, x is the path length of the X-rays through the object and μ is the linear attenuation coefficient. This coefficient depends on the energy of the X-rays, as well as the density and atomic composition of the material. For most materials and commonly used values of energy, the linear attenuation coefficient is generally given by the simplified equation:

$$\mu = \rho(a + bZ^{3.8}/E^{3.2}) \tag{2}$$

where ρ and Z are the density and the atomic number of the object, respectively, and E is the energy of the X-rays. The quantities a and b appearing in Equation (2) are instrument-dependent parameters [9].

The units of a 3D image obtained through XR-CT are called voxels. A voxel is a volume element representing, in three-dimensional space, the mean value of the opacity of material to X-rays.

Experimental set-up

The system used in this research allows performing microtomography of a specimen under load (*in situ*), using a specifically built load frame that could be placed in the X-ray beam. To the best of the authors' knowledge, *in situ* synchrotron radiation microtomography is used here for the first time for saturated rock. The experimental programme needed both *fast scanning* (the specimen was scanned while the axial strain was held constant, which unavoidably causes some amount of axial load relaxation during scanning; the shorter the scanning time, the smaller this relaxation) and *high accuracy* (because the zones of strain localisation are extremely thin in a fine-grained material). Among the three types of scanners available (medical and industrial scanners and synchrotron), synchrotron radiation was selected because it is the only one which combines short scanning time and high resolution – due to the high photon flux. More precisely, the experiments were carried out at the high-energy beamline ID15A at the ESRF [10]. Figures 1 and 2 show the experimental set-up and Figure 3 details the scanning configuration. The X-ray beam used was a white beam to have the highest photon flux available, and was generated by a 11-pole wiggler. Note that the beam was filtered (hardware) to remove low-energy photons, which allows avoiding beam-hardening artefacts. The X-ray energy used in this study ranges from 50 to 70 keV, allowing going through the confinement cell, the confining fluid and the specimen. The optical system was composed of a phosphor screen which transforms X-ray into visible light, a 1× objective and a Dalstar CCD camera (1024 × 1024 pixels; DALSA, Waterloo, ON, Canada) which has a short acquisition time. A complete scan was obtained by recording 1200 measurements at different angles equally spaced on 180°. The exposure time for each measurement was 0.04 s. The spatial resolution (i.e. the voxel size in the reconstructed slice) is $14 \times 14 \times 14$ μm^3. The field of view (i.e. the beam section size) was 14 mm wide in order to cover the specimen and 3.65 mm in thickness. During each scan, 261 contiguous slices were recorded at the same time. Such a stack of slices is hereafter referred to as a *section*. A section was recorded in approximately 2.5 min. The acquisition of the entire specimen (which was 10 mm in diameter and 20 mm in height) required six sections and took no more than 15 min. These 3D sub-images are concatenated into

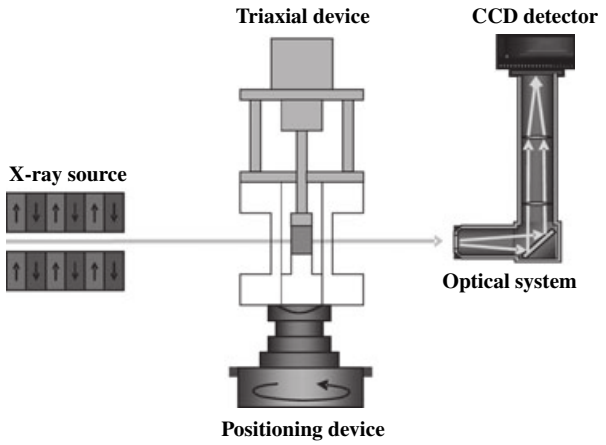

Figure 1: Schematic of the X-ray microtomography set-up for triaxial testing

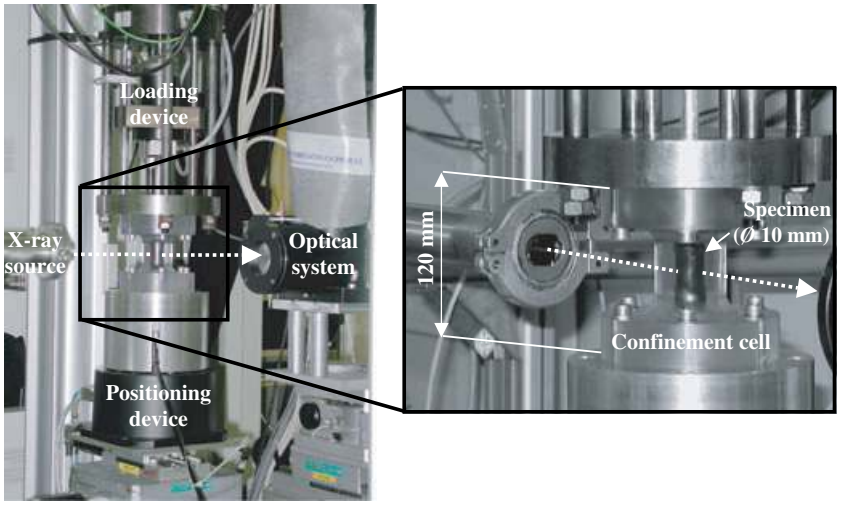

Figure 2: Tomography set-up for triaxial testing at the beamline ID15A at ESRF. Complete set-up on the beamline (left) and zoom on the rock specimen inside the triaxial cell (right)

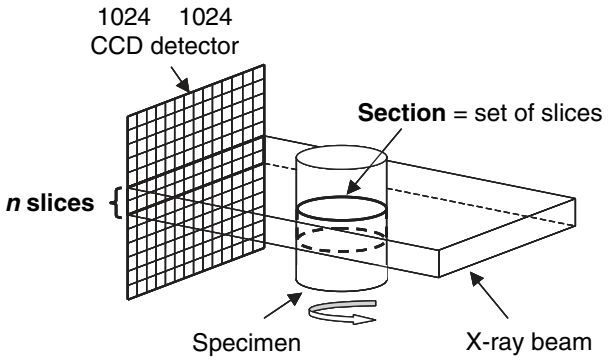

Figure 3: X-ray beam through the specimen to the phosphor screen

one large image, representing the whole specimen, including the rubber jacket. Typical size of such images is 925 × 925 × 1325 voxels.

The apparatus includes a small triaxial cell and a loading device designed specifically for performing microtomography on clays and argillaceous rocks under loading [6, 11]. The triaxial apparatus is practically the same as a conventional triaxial testing system, except for its much smaller size and the shape of the confining cell, which was designed to be as transparent as possible to the X-rays. A 10-mm-thick confining cell made of polycarbonate was used, which is both transparent to the X-rays and capable to sustain the 10 MPa confinement pressure and the tensile reaction force. The axial load and hence the deviator stress are applied in a displacement-controlled manner using a motor-driven screw actuator. The loading system, which can be placed in the X-ray beamline without interfering with the tomographic scans, is quite compact and light, which is important because it sits directly on the translation and rotation stage during the experiment. The system has a maximum loading capacity of 7.5 kN, and allows to move the ram at a constant rate in the range of 1–100 μm min^{-1}.

Tested material

The material tested for this study is the Callovo-Oxfordian argillite issued from the ANDRA Underground Research Laboratory located at Bure (Meuse/Haute Marne, Eastern France) at approximately 550 m below the ground surface. It is a sedimentary rock composed of particles of calcite and quartz in a clay matrix (interstratified illite/smectite, illite, chlorite). The clay fraction is 40–45%, while carbonate (essentially calcite) and quartz represent about 25–35% and about 30%, respectively; other minerals can also be found, namely feldspar, mica and pyrite. Clay particles are clustered into aggregates which are globally oriented along the stratification, whereas the other mineral inclusions have no preferential orientation, except some vein-shaped calcite inclusions that are also oriented along the stratification. At the investigated depth, the material has an extremely low permeability (10^{-20}–10^{-22} m^2), a porosity of 15% and a water content of 6%. The uniaxial compressive strength is about 20 MPa.

Digital Image Correlation Applied to 3D Images

Background

Quantitative information on local strain distribution can be obtained by the detailed comparison of XR-CT images of the sample recorded at various load steps. Two-dimensional DIC techniques were developed in the late 1980s in the field of solid and fluid mechanics [12, 13] and numerous applications at various space and time scales, on various materials and structures and for different loading conditions, are now reported. Basically, they consist in finding the homologous positions of a set of material points in two or more images, by optimising a correlation coefficient that measures the similarity of the grey-level distribution in a small domain around these points, assuming that this distribution is convected by the material transformation according to some optical flow conservation principle. Their extension to three-dimensional images [14, 15] is straightforward when such a local image contrast is available and obeys such a conservation principle, at the only cost of longer but nowadays affordable computations. First reported applications were concerned with the macroscopic deformation of bones [16] imaged with macro-XR-CT. Such materials are appropriate for such investigations because of their low absorption properties and the availability of a natural contrast provided by their porous microstructure. Investigations on denser materials and at smaller scales may require XR-CT images recorded using synchrotron radiation. The investigation of the deformation of metallic samples made of an aluminium alloy in which small cupper inclusions were embedded to provide the appropriate contrast for the pattern matching is reported in Ref. [17], where images with a spatial resolution of 2 μm were used; the resolution of the pattern matching algorithm, as evaluated from the analysis of rigid body motions, was close to 0.01 voxels (standard deviation) in optimal imaging conditions, but could substantially

be degraded by the presence of noise or reconstruction artefacts in the images. Strain levels ranging from 0.2% to 20%, on gauge lengths of about 60 μm, in samples with millimetric cross-sections could be measured. The same implementation of the 3D-DIC algorithms has been used in the present study, but on very different materials and with less favourable imaging conditions. In the next sections, the main lines of the used DIC procedure are recalled; additional information can be found in Refs [14, 15, 17]. The suitability of the images for 3D-DIC will also be discussed.

General principles

A standard DIC technique is characterised by the definition of the correlation coefficient $C(\Phi)$, the description of the local transformation Φ that maps the correlation window D in the reference image to the deformed image, and the type of interpolation that allows for a subvoxel evaluation of the displacement field. Let $f(x)$ and $g(x)$ be the grey level at point x in the reference and deformed images, respectively. The similarity of the window D and its transformed $\Phi(D)$ can be measured by the so-called zero centred normalised cross-correlation coefficient:

$$\begin{aligned} C(\Phi) &= 1 - \frac{\langle (f - \langle f \rangle) \cdot (g \circ \Phi - \langle g \circ \Phi \rangle) \rangle}{\sqrt{\left\langle (f - \langle f \rangle)^2 \right\rangle \cdot \left\langle (g \circ \Phi - \langle g \circ \Phi \rangle)^2 \right\rangle}} \\ &= 1 - \frac{\langle f \cdot g \circ \Phi \rangle - \langle f \rangle \cdot \langle g \circ \Phi \rangle}{\sqrt{\left(\langle f^2 \rangle - \langle f \rangle^2 \right) \cdot \left(\left\langle (g \circ \Phi)^2 \right\rangle - \langle g \circ \Phi \rangle^2 \right)}} \end{aligned} \tag{3}$$

where $\langle a \rangle$ is the average of scalar a over D and $g \circ \Phi(x) = g(\Phi(x))$. It varies from 0 (perfect match) to a maximum of 2 (when fluctuations of f and g are opposite), the value 1 corresponding to no match at all. This measure of similarity is insensitive to a global contrast or brightness variation on the windows between both configurations. Even if in principle XR-CT images are 3D representations of local linear attenuation coefficients, which can be defined on an absolute scale, such fluctuations can in practice be observed because of instrument imperfections or various image manipulations. In particular, the voxel grey levels of the images obtained after reconstruction, which are represented by 32-bit single precision floating point numbers, are rescaled into 8-bit integers for 3D-DIC and visualisation, in order to limit disk and memory usage. This conversion is in general based on a linear look-up table, with upper and lower thresholds chosen such as to emphasise the available contrast used for pattern matching. Variations of these thresholds between the configurations can induce global brightness and contrast changes.

Images being discrete representations of continuous attenuation coefficient distributions, the averages are approximated by sums over the N voxels in the usually cubic domain D:

$$\langle a \rangle \approx \frac{1}{N} \sum_{\text{voxels } ijk \text{ in } D} a_{ijk} \tag{4}$$

where a_{ijk} is the value of a at position (i,j,k). As $\Phi(i,j,k)$ might not be an integer position in the deformed image, the computation of $(g \circ \Phi)_{ijk}$ requires an interpolation, which for the present application is a continuous trilinear interpolation of the grey levels of the eight first neighbour voxels of the position $\Phi(i,j,k)$. For the present application, the transformation Φ was assumed to be a simple translation, characterised by its three components and computations were performed in real space (i.e., without fast Fourier transform technique). Higher order transformations could have been used, but with probably no significant improvement of the results in areas where strains are small. In addition, they may have failed in regions of the specimen experiencing localised deformation, because of possible local displacement discontinuities and strong evolutions of the local grey-level distributions, due to local damage induced by localised deformation, such that the optical flow conservation principle would no longer apply. The questions relative to a better description of localised deformation within DIC windows are left for further investigations. In this study, rather standard DIC techniques are used for the detection of such areas, with a spatial resolution given by the size of the correlation windows and the spacing of the discrete positions at which the displacement is evaluated, which are taken equal.

Practical procedure

Single increment.

In practice, the 3D-DIC procedure is split into four steps. The first is the construction of the initial integer positions in the reference image, which are distributed on a regular mesh of a parallelepiped that encompasses the cylindrical sample and is defined by the positions of four manually selected vertices. Only positions inside the sample are analysed. They are selected semi-automatically on the basis of the average grey level in a small surrounding window and an appropriate threshold, which is easy to select as the attenuation coefficient of the argillaceous rock is significantly larger than that of the surrounding confining cell. This

leads to the definition of a cylindrical region of interest (ROI), which maps to the whole sample and contains typically several 10 thousands of reference positions.

The second step is a first determination of their homologous positions in the deformed image, performed semi-automatically and sequentially. An approximate position of a new point, deduced from that of an already found near neighbour by assuming a homogeneous local transformation, is optimised by a systematic computation of $C(\Phi)$ for all integer translations leading to a surrounding 'exploration window' of size $s_x \times s_y \times s_z$ voxels. The correlation window D relative to reference position (i,j,k) is centred on this position, such that the lower and upper column indices of voxels in D are $i - E[(n_x-1)/2]$ and $i - E[(n_x - 1)/2]+n_x - 1$, respectively, $E[a]$ being the integer part of a and n_x the – even or odd – window width. Similar conventions hold for the row and plane indices. If the minimum of $C(\Phi)$ is below a given threshold, the optimal position is retained and the next point is sought. If not, a manual positioning is requested, which may or may not be reoptimised, depending on the choice of the operator. A similar manual positioning is used for the first point. When no positioning is possible because of the lack of local contrast, a too strong evolution of it, or the presence of reconstruction artefacts which mask the contrast, the operator may choose to eliminate the corresponding point from the ROI. No subvoxel optimisation is performed at this stage, in order to accelerate the treatment. The numerical complexity is of the order $n_x n_y n_z s_x s_y s_z$, so that appropriate correlation and exploration window sizes need to be selected in order to reduce the computation time.

The fully automatic third step consists in applying the subvoxel optimisation procedure described in Ref. [17] to all positions at which the correlation coefficient is below a given threshold. This is based on a first gradient minimisation and the trilinear interpolation of grey levels mentioned above. Steps 2 and 3 can be performed at a same time, but at the price of a longer computation time and a possible waste of time for the operator. These first three steps are implemented[1] in the CORRELMANU3D software. Its graphical interface makes possible the interactive control of the process and in particular a precise superposition of corresponding CT slices. It was run on a 64-bit Linux workstation with 8 GB of main memory. The new capabilities offered by 64-bit systems are here very useful as they allow one to keep the two large CT images (1.3 GB each in the present case) in main memory without any specific computational strategy.

The final step aims at computing strain components. A regular finite element mesh made of eight-node trilinear elements is constructed. The nodes coincide with the measurement positions in the reference image, but only those elements for which the displacement at all eight nodes could be determined are defined. Figure 4 shows the obtained mesh, with some missing elements near the centre of the sample, where the high concentration of ring artefacts did not allow a satisfactory determination of the displacement field. The nine components of the average deformation gradient in each element, as well as all quantities derived from these, are computed by means of the finite element (FE) software CAST3M. The recourse to such an FE package results first from practical concerns: it provides various efficient post-processing tools for the analysis of 3D tensorial field data, which would have been rather tedious to develop from scratch. In addition, the computation of strain tensor components from discrete displacement data by means of finite element shape functions provides a clear interpretation of local strain values. More precisely, when strains are averaged over the elements (not computed at Gauss integration points), the obtained values are strains relative to a well-defined local gauge length, given by the size of the elements. Alternative procedures based on polynomial interpolation would generate local values which might be less noisy, but would be strongly dependent on the interpolation procedure, with a less clearly defined local gauge length. According to the adopted

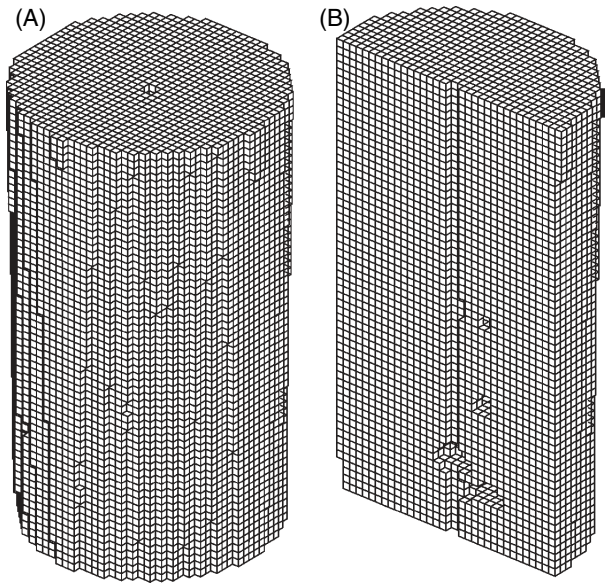

Figure 4: FE mesh for post-processing, made of 54 193 elements and 60 819 nodes: (A) global view; (B) vertical cut showing some missing elements, close to the rotation axis

[1]The procedures used for the subvoxel optimisation are due to P. Doumalin.

small strain framework, which is sufficient in non-localised areas where deformations are small, the strain tensor ε is the symmetric part of the transformation gradient. Its trace gives the volumetric strain and the classical von Mises equivalent strain $\varepsilon_{\text{eq}} = \sqrt{\frac{2}{3}\text{dev}(\varepsilon) : \text{dev}(\varepsilon)}$, where $\text{dev}(\varepsilon)$ is the deviator of ε, measures the shear strain. In principle, these quantities are not appropriate in the regions of localised deformation, where strains are high. But in the present work, they are mainly used as indicators of the presence of localisation, and not as exact measures of the intensity of localised strain.

Multiple increments.

The second and third steps are repeated for each of the deformed stages. It might, however, be more efficient to use as reference configuration the previous deformed stage instead of the first undeformed one, in order to facilitate the processing of highly deformed areas where the local contrast evolves strongly. The reference image is then that of the previous deformation stage and the reference points are the positions obtained from the 3D-DIC procedures at the previous stage. Steps 2 and 3 can then be run as described above, with two exceptions: positions that could not be analysed in the previous stages are removed from the ROI, and reference positions do no longer have integer coordinates. Let (x_p,y_p,z_p) be the coordinates of the pth reference point and (i_p,j_p,k_p) their integer parts. The described procedures can be used to compute the homologous of point (i_p,j_p,k_p) in the next configuration, or more generally the optimal transformation Φ that maps the window D centred on (i_p,j_p,k_p) to the next image. The new position of point (x_p,y_p,z_p) in the next configuration is then computed as $\Phi(x_p,y_p,z_p)$. With such a methodology, in which positions are recorded instead of translation vectors, one can easily compute not only total strains but also incremental strains between any pair of configurations. This is particularly useful for the detection of active mechanisms.

Image characteristics and accuracy

The local grey-level fluctuations required by 3D-DIC algorithms result from the heterogeneous microstructure of the investigated rocks, made of constituents with different attenuation coefficients, as described in the 'Tested material' section. However, the differences in attenuation are small, so that the ratio of spatial signal fluctuation to noise is low. In addition, the size of the mineral inclusions, typically below 50 μm, is close to the spatial resolution of the CT images, so that only the larger ones can be seen, although only roughly discretised. There are few larger inclusions with higher attenuation coefficients, which appear as white inclusions, but their distribution is sparse. In most correlation windows, only the low contrast of poorly discretised small inclusions is available. Figure 5 shows an enlarged detail of a CT slice, the grey-level histogram within a typical 20^3 voxels correlation window as well as a 1D

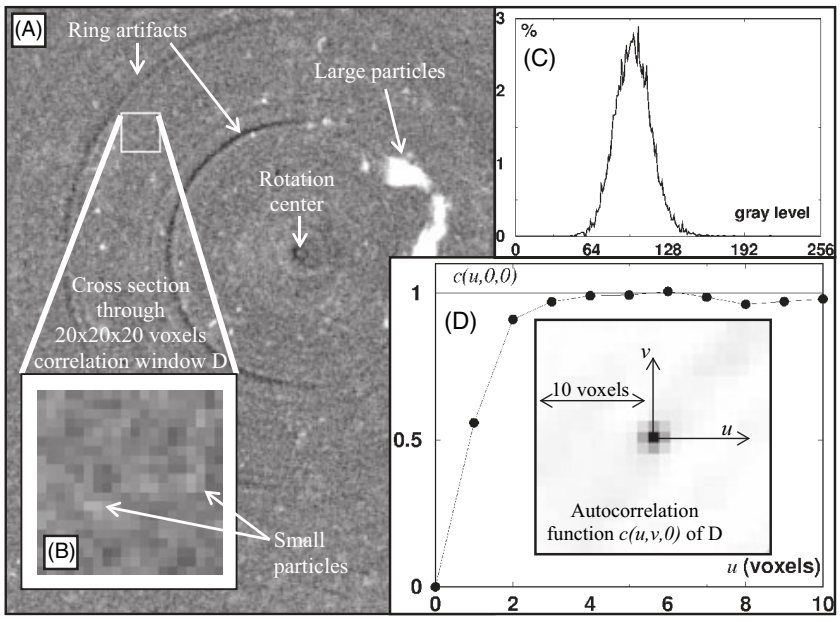

Figure 5: Image characteristics: (A) detail of typical CT slice of the sample showing ring artefacts and large particles, (B) enlarged cross-section through typical correlation window showing actual contrast used for 3D-DIC, (C) corresponding grey-level histogram and (D) autocorrelation function (unidirectional profile and 2D cross-section). The autocorrelation function $c(u,v,w)$ is given by $C(\Phi)$ when Φ is the translation with components (u,v,w) and deformed image coincides with reference image

profile and a 2D cross-section of the 3D-autocorrelation function of such a window, as defined in the figure caption. Subvoxel accuracy of 3D-DIC depends on the width of the grey-level histogram relative to the standard deviation of noise and on the appropriate discretisation of the autocorrelation function, which determines interpolation errors. In the present case, the radius of the autocorrelation well is probably too small, being less than two voxels, and the grey-level distribution is rather narrow. The latter can be enlarged by the use of another look-up table during the floating point numbers to 8-bit integers conversion. Three different tables have been tested, including a nonlinear one which aimed at avoiding saturation effects, but without significant modifications on the results. This suggests a limitation due to the intrinsic signal-to-noise ratio in the initial 32-bit floats CT images. These two image characteristics indicate a relatively poor performance of the available local contrast for DIC, with respect to previous studies. Another indication is the value of the optimal correlation coefficient, which was in the range 0.3–0.5, while values below 0.1 were obtained on other images like those reported in Ref. [17]. The recourse to higher spatial resolutions and longer exposure times might improve the measurements, but with the risk of biases due to relaxation.

The 3D-DIC algorithms were applied anyway, with 20^3 voxels windows. A clear correlation minimum could be found at almost all points in the sample, except in areas with strong reconstruction artefacts or with localised deformation. In the latter case, manual positioning was often necessary. As the local contrast has a small characteristic size, as indicated by the autocorrelation function well, smaller correlation windows could probably have been used. However, in order to limit the number of measurement points to a reasonable value (more than 60 000 in the present case), the pitch of the regular grid of the measurement points was set to 20 voxels and the correlation window size chosen accordingly, in view of taking advantage of all the information available in the CT images.

The actual accuracy of the positioning of homologous points is hard to evaluate. It is probably better than one voxel, as strain maps after subvoxel optimisation reveal smoother strain distributions than those obtained without optimisation, in which classical moiré fringes due to rounding effects can be seen. On the other hand, the standard deviation of the errors on displacements, σ_u, is certainly larger than 0.01 voxel, which is the value obtained in Ref. [17] with more appropriate images. The analysis of rigid body motions would provide a first evaluation of this error but has not yet been performed. The standard deviation of errors on strain components is of the order of $\sigma_u/L/\sqrt{m}$, where L is the strain gauge length and m the number of independent relative displacement measurements used in the strain calculation. For local strain values, computed as the strain average in the trilinear finite elements, L is equal to 20 voxels and equivalent m value is 4, so that the accuracy on local strains is close to 0.01. This is not a good accuracy, yet it is more than sufficient to detect localised regions where strain can reach large values. The standard deviation of the overall strain components evaluated similarly is better than 10^{-4}, because of the long gauge length ($L = 1300$) and the large number of independent measurements ($m = 1000$).

Discussion and Analysis of the Results

Direct observation of tomographic images

The main results of the triaxial program have been thoroughly discussed elsewhere [11, 18]. The present paper focuses on 3D-DIC and the extra advantages that it provides as compared with the simple observation of tomographic images. However, it is necessary to discuss first a few such images.

As an example, let us consider a few images from test *ESTSYN01*. Figure 6 shows the deviator stress versus axial strain during this test, performed with a cell pressure of 10 MPa. The numbers noted on the curve are the scanning step numbers. Eight 3D complete images of the specimen were recorded, the

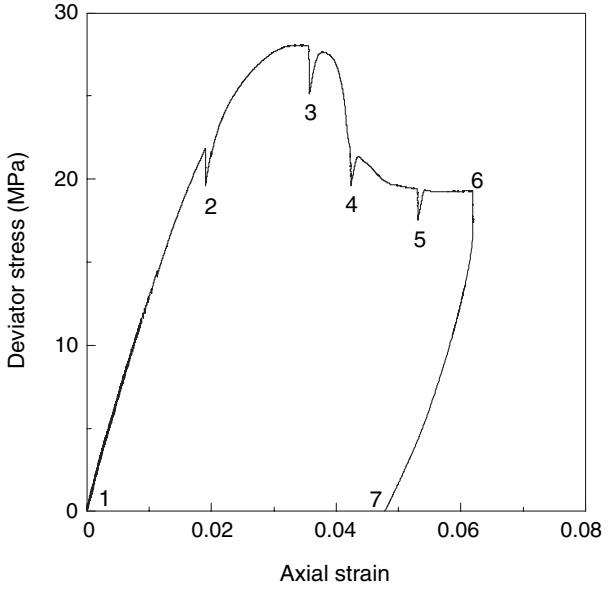

Figure 6: Deviator stress versus axial strain response recorded during test *ESTSYN01* (10 MPa confining stress)

last of which (not noted on the curve) was recorded at the end of the test, after removal of the confining pressure. Figure 7 shows four horizontal CT slices extracted from the 3D images of specimen *ESTSYN01* at different steps. The slices at steps 3, 7 and 8 have been selected following a set of material points which were visible at step 1 and could be found on all subsequent images.

At step 8, two open cracks can be seen on the specimen edges. Comparison of the images at steps 7 and 8 clearly indicates that crack opening in this test was essentially due to the removal of the confinement pressure. At the earlier step 3, which corresponds to the peak stress, no sign of localised deformation can be detected – even knowing where the cracks are eventually opening up later in the test. Furthermore, no visible difference can actually be found between the two slices at steps 1 and 3.

It is interesting to compare the images of Figure 7 with one CT slice recorded during test *ESTSYN02*, which was performed at a much lower confining pressure (1 MPa). The image shown in Figure 8, which corresponds to a state just after the peak deviator stress, shows a very different scenario: several open cracks are already present at the peak state, clearly indicating the localised nature of the deformation process. This is significantly different from test *ESTSYN01*, for which localisation became clearly visible only after the removal of the confinement pressure.

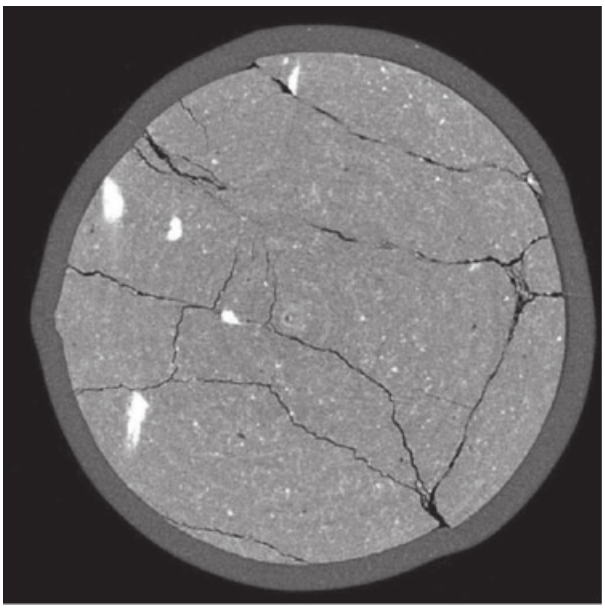

Figure 8: Horizontal CT slice of specimen *ESTSYN02* just after the peak deviator stress

The above discussion illustrates a fundamental limitation of XR-CT as a tool to detect strain localisation *directly* from the observation of the tomo-

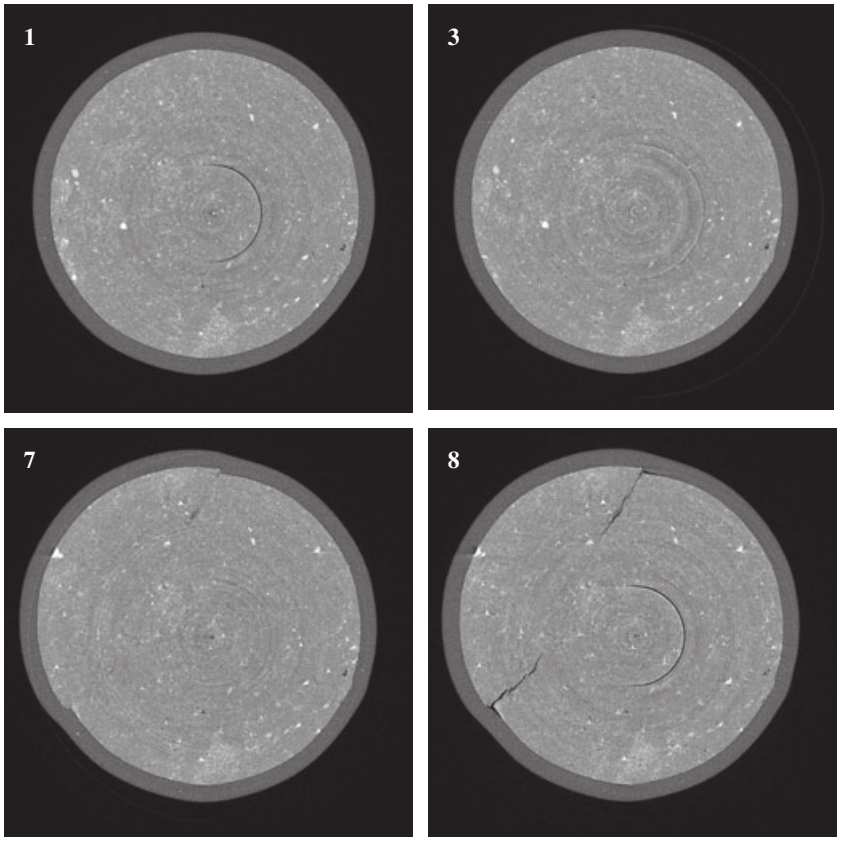

Figure 7: Horizontal CT slices of specimen *ESTSYN01* at four different steps

graphic images. In fact, as these images represent local mass density fields, they only provide *direct* information about: (i) the internal geometry of the specimen, including any heterogeneities, either diffuse or localised (inclusions) at a given step of the test and (ii) the local mass density variations (either diffuse or localised) from one step to another. If the material inside the region of localised deformation dilates (or contracts), then local mass density variations are an effective means to track the regions of localised deformation (provided that the volumetric strain in these regions is large enough to result in measurable variations of mass density and hence of X-ray attenuation). This was the case with previous studies of shear banding in sand (e.g. [4, 19]). As far as the present study is concerned, this is certainly the case with open cracks, where voids are created between the crack edges that are clearly visible on the tomographic images (e.g. step 8 in Figure 7, and Figure 8). However, if the localised deformation is essentially isochoric (no volume change), or if it consists of closed, shearing cracks, it is hidden to the direct observation of CT images.

Overall, it can be concluded that using mass density changes to detect shear strain localisation is in fact an *indirect* method, which proves to be effective only in some particular cases. On the contrary, as it will be shown in the next section, the correlation of 3D digital images from X-ray tomography provides a *direct* means to detect (within a given accuracy) any localised deformation, independent of its nature (shear or volumetric strain).

3D-DIC results

3D-DIC was used in this study to obtain the spatial displacement of a set of points from one 3D image to another, and then the corresponding (incremental) strain field. It is convenient to represent these results by the invariants of the strain tensor. Herein, we use

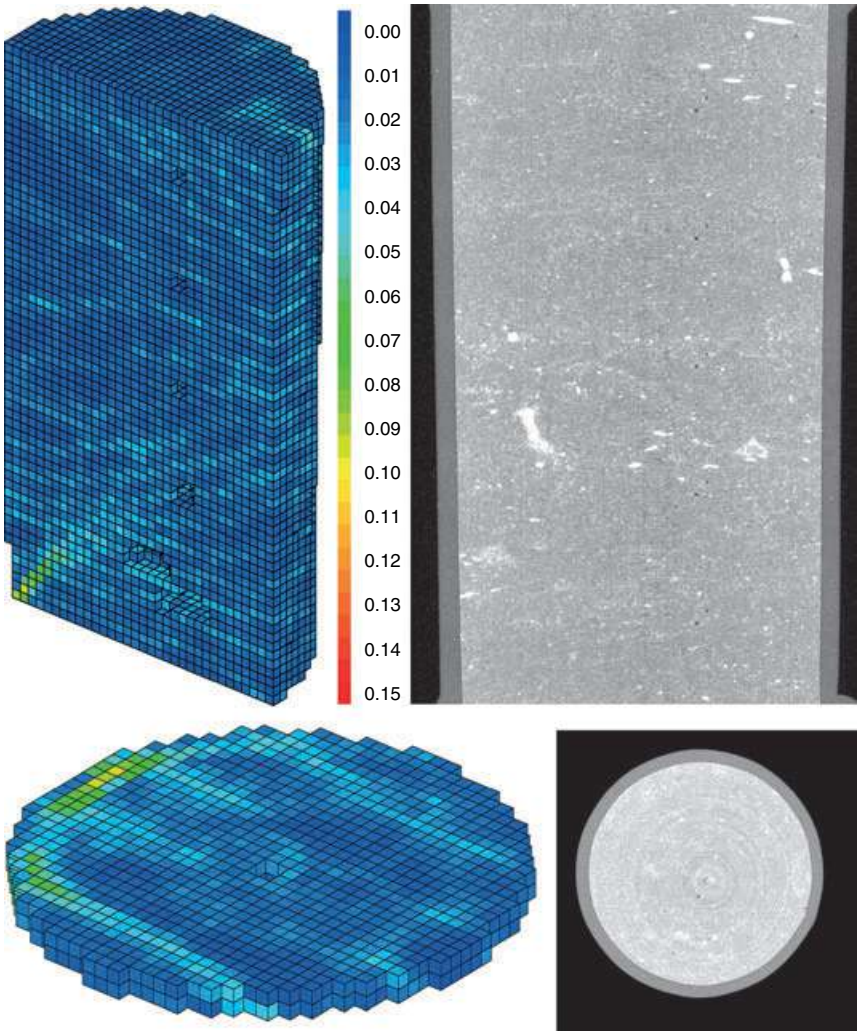

Figure 9: Deformation increment 2–3 of test ESTSYN01. Vertical cut along the axis of the specimen (top) and horizontal cut close to the bottom end of the specimen (bottom). Left: deviatoric incremental strain (strain averaged over the elements: local gauge length is 280 μm); right: radiographic cut at step 3, i.e. at the peak deviator stress. The colour scale covers the range [0, 0.15]

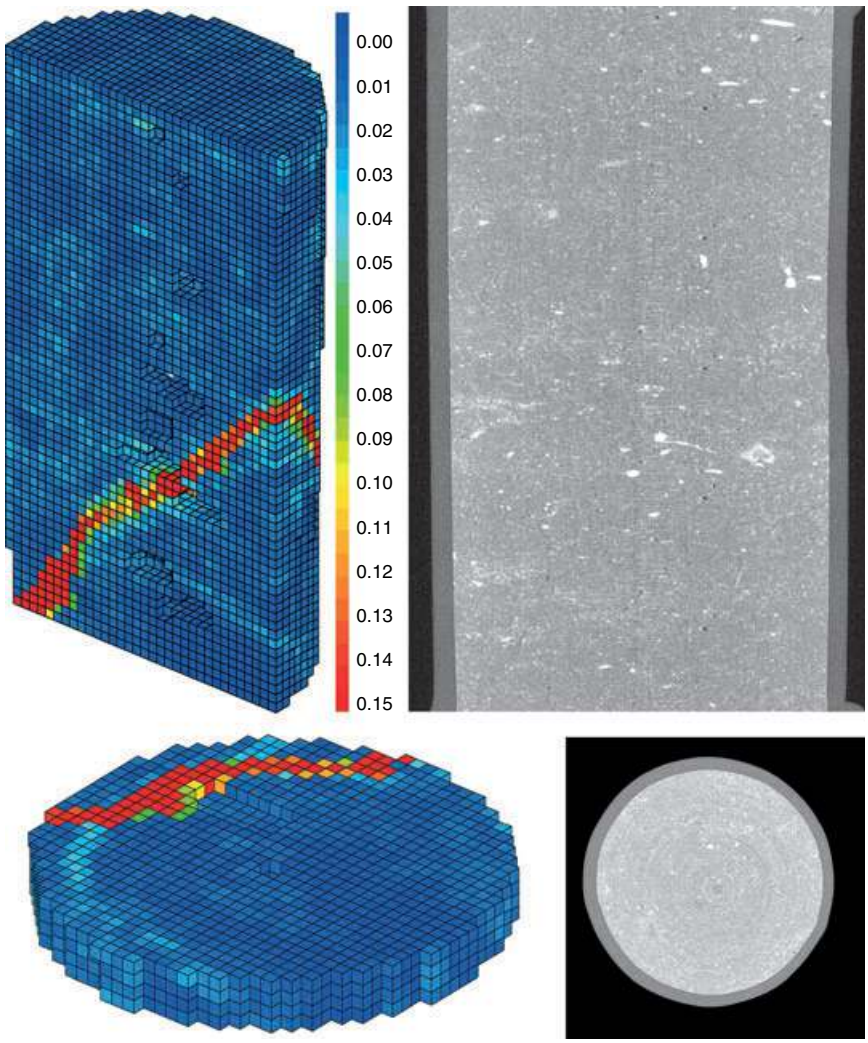

Figure 10: As Figure 9, but deformation increment 3–4

the von Mises equivalent strain (cf. 'Digital image correlation applied to 3D images'), which is a measure of shear strain. The images on the left side of Figures 9 and 10 show a few such strain fields as obtained for specimen *ESTSYN01*, where each 3D subset (constant strain element) contains 20^3 voxels. In other terms, the gauge length used to define (and compute) the strain was equal to 20 voxels, or 280 μm, in each of the three spatial directions. The computed 3D fields are shown by vertical (top of Figure 9 and 10) and horizontal (bottom of the same figures) cuts.

In the pre-peak increment (2–3), the onset of strain localisation can be distinctly detected in the strain maps as a small clear oblique band at the left bottom corner of the vertical cut (Figure 9, leftside, top). The horizontal cut (Figure 9, x2, left side, bottom) shows that, at this stage, localisation developed with a conical shape. These features can clearly be distinguished from the moiré fringes that spread all over the sample and which are highly likely to be induced by systematic errors of the DIC algorithm associated with grey-level interpolation and rounding effects. On the other hand, the radiographic sections of specimen at the end of the increment (shown on the right side of the figure) do not reveal any trace of localised deformation.

In the post-peak increment (3–4), Figure 10 shows a fully developed shear band through the specimen. As compared with the pre-peak increment, the zone of localised deformation appears straight (planar) both in the vertical and in the horizontal cuts. A closer comparison of the images for the two increments reveals that the post-peak localisation band coincides with the pre-peak cone of localised deformation in the lower region, although it departs from it at some elevation from the bottom of the specimen. As already observed for the previous increment, direct observation of the radiographic cuts of the specimen at the end of the increment (see right side of Figure 10) fails in revealing any sign of this region of strain localisation.

In summary, these 3D incremental strain fields suggest that a region of localised shear strain formed in the specimen already prior to the deviator stress peak. While the shape of such a region was conical in this early stage, a more planar mechanism developed in the subsequent increment, after the peak. Although geometrically different, the latter shear zone was likely driven by the former zone of localisation. Finally, it is worth to note that the thickness of the shear bands as it appears in these DIC-based shear strain fields is largely over-evaluated, because it cannot be smaller than the subset size. Recall that the side of the subset was equal to 20 voxels (i.e. 280 μm) in this analysis, whereas CT images indicate that the thickness of the zones of localised deformation (be these dilating shear bands or open cracks) in the tested specimens was typically less than 70 μm (see Ref. [11]).

Conclusion

An original experimental device has been developed for testing argillaceous rocks at relatively high confining pressures (10 MPa), which allows for microtomography observation of the specimen under deviatoric loading. The objective of this study was to evaluate the onset and evolution of localised deformation throughout a test. High-energy synchrotron radiation was used, which allowed for both *fast* and *high-resolution* microtomography.

It was shown that localisation patterns observable using only direct examination of the tomographic images are limited and not representative of all the localised deformation taking place in the specimens. In fact, only deformation processes involving local changes in bulk density can be directly detected from these images.

However, it has been shown in this study that X-ray 3D imaging can be effectively complimented with Volumetric Digital Image Correlation, which allows obtaining 3D strain fields of the deforming specimen at different loading steps. The quality of the results crucially depends on the quality of the images (which need to be well contrasted) as well as on the signal-to-noise ratio, which must be sufficiently high. In this study, while the use of synchrotron light allowed meeting the latter requirement, the contrast in the images directly results from the natural heterogeneity of the tested material.

The results obtained with Volumetric Digital Image Correlation revealed patterns of localisation which could not be observed only based on the 3D tomographic images and remained therefore hidden to the experimentalist despite the high resolution and efficiency of the microtomographic installation.

In the authors' opinion, the application of Volumetric Digital Image Correlation to images obtained through X-ray tomography will certainly become a major tool for material science and experimental mechanics in the near future.

ACKNOWLEDGEMENTS

The authors are very grateful to Marco Di Michiel from the ESRF at Grenoble for his invaluable contribution to the experimental program. We also wish to thank ANDRA for financially supporting this project and for supplying core samples from their site at Bure, France. This work was performed within the French CNRS research network 'GDR 2519 – Mesure de champs et identification en mécanique des solides'.

REFERENCES

1. Vardoulakis, I. and Sulem, J. (1995) *Bifurcation Analysis in Geomechanics*. Blackie, Glasgow.
2. Desrues, J. (1998) Localization patterns in ductile and brittle geomaterials. In: *Material Instabilities in Solids* (R. de Borst and E. van der Giessen, Eds). Wiley-Interscience, Chichester: 137–158.
3. Desrues, J. and Viggiani, G. (2004) Strain localization in sand: an overview of the experimental results obtained in Grenoble using stereophotogrammetry. *Int. J. Numer. Anal. Methods Geomech.* **28**, 279–321.
4. Desrues, J., Chambon, R., Mokni, M. and Mazerolle, F. (1996) Void ratio evolution inside shear bands in triaxial sand specimens studied by computed tomography. *Geotechnique* **46**, 529–546.
5. Desrues, J. (2004) Tracking strain localization in geomaterials using computerized tomography. In: *X-ray CT for Geomaterials* (J. Otani and Y. Obara, Eds). Lisse, Balkema: 15–41.
6. Viggiani, G., Lenoir, N., Bésuelle, P., Di Michiel, M., Desrues, J. and Kretzschmer, M. (2004) X-ray micro tomography for studying localized deformation in fine-grained geomaterials under triaxial compression. *C. R. Mec. Acad. Sci.* **332**, 819–826.
7. Mees, F., Swennen, R., Van Geet, M. and Jacobs, P. (2003) *Applications of X-ray Computed Tomography in Geosciences*. GSL Special Publication. Geological Society of London.
8. Otani, J. and Obara, Y. (2004) *X-ray CT for Geomaterials* (J. Otani and Y. Obara, Eds.). Balkema: Lisse.
9. Curry, T. S., Dowdey, J. E. and Murry, R. C. (1990) *Christensen's Physics of Diagnostic Radiology*. Lea and Febiger, London, 522 pp.
10. Di Michiel, M., Merino, J. M., Fernandez-Carreiras, D., Buslaps, T., Honkimäki, V., Falus, P., Martins, T. and Svensson, O. (2005) Fast microtomography using high energy synchrotron radiation. *Rev. Sci. Instrum.* **76**, 043702.

11. Lenoir, N. (2006) *Mechanical behavior and rupture of clayey rocks studied by X-ray micro tomography*. PhD thesis. University of Grenoble I, in French, available online http://tel.ccsd.cnrs.fr/tel-00011996.

12. Chu, T., Ranson, W., Sutton, M. and Peters, W. (1985) Applications of the digital-image-correlation techniques to experimental mechanics. *Exp. Mech.* **25**, 232–244.

13. Kimura, I. and Takamori, T. (1986) Image processing of flow around a circular cylinder using cross correlation technique. *Flow Vis.* **IV**, 221–226.

14. Bay, B. K., Smith, T. S., Fyhrie, D. P. and Saad, M. (1999) Digital volume correlation: three-dimensional strain mapping using X-ray tomography. *Exp. Mech.* **39**, 217–226.

15. Smith, T. S., Bay, B. K. and Rashid, M. M. (2002) Digital volume correlation including rotational degrees of freedom during minimization. *Exp. Mech.* **42**, 272–278.

16. Verhulp, E., Van Rietbergen, B. and Huiskes, R. (2004) A three-dimensional digital correlation for strain measurements in microstructures. *J. Biomech.* **37**, 1313–1320.

17. Bornert, M., Chaix, J. M., Doumalin, P., Dupré, J. C., Fournel, T., Jeulin, D., Maire, E., Moreaud, M. and Moulinec, H. (2004) Mesure tridimensionnelle de champs cinématiques par imagerie volumique pour l'analyse des matériaux et des structures. *Instrum. Mes. Metrol.* **4**, 43–88.

18. Bésuelle, P., Viggiani, G., Lenoir, N., Desrues, J. and Bornert, M. (2006) X-ray micro CT for studying strain localization in clay rocks under triaxial compression. In: *Advances in X-ray Tomography for Geomaterials* (J Desrues, G. Viggiani and P. Besuelle, Eds.). ISTE Ltd, London: 35–52.

19. Alshibli, K. A., Sture, S., Costes, N. C., Frank, M., Lankton, M., Batiste, S. and Swanson, R. (2000) Assessment of localized deformations in sand using X-ray computed tomography. *ASTM Geotech. Test. J.* **23**, 274–299.